JBC RESEARCH ARTICLE

Receptor-binding domain of SARS-CoV-2 is a functional αv-integrin agonist

Received for publication, April 12, 2022, and in revised form, January 10, 2023 Published, Papers in Press, January 18, 2023,
https://doi.org/10.1016/j.jbc.2023.102922

Emma G. Norris[1], **Xuan Sabrina Pan**[2], **and Denise C. Hocking**[1,2,*]

From the [1]*Department of Pharmacology and Physiology, University of Rochester School of Medicine and Dentistry, Rochester, New York, USA;* [2]*Department of Biomedical Engineering, University of Rochester School of Medicine and Dentistry, Rochester, New York, USA*

Reviewed by members of the JBC Editorial Board. Edited by Craig Cameron

Among the novel mutations distinguishing SARS-CoV-2 from similar coronaviruses is a K403R substitution in the receptor-binding domain (RBD) of the viral spike (S) protein within its S1 region. This amino acid substitution occurs near the angiotensin-converting enzyme 2–binding interface and gives rise to a canonical RGD adhesion motif that is often found in native extracellular matrix proteins, including fibronectin. Here, the ability of recombinant S1-RBD to bind to cell surface integrins and trigger downstream signaling pathways was assessed and compared with RGD-containing, integrin-binding fragments of fibronectin. We determined that S1-RBD supported adhesion of fibronectin-null mouse embryonic fibroblasts as well as primary human small airway epithelial cells, while RBD-coated microparticles attached to epithelial monolayers in a cation-dependent manner. Cell adhesion to S1-RBD was RGD dependent and inhibited by blocking antibodies against α_v and β_3 but not α_5 or β_1 integrins. Similarly, we observed direct binding of S1-RBD to recombinant human $\alpha_v\beta_3$ and $\alpha_v\beta_6$ integrins, but not $\alpha_5\beta_1$ integrins, using surface plasmon resonance. S1-RBD adhesion initiated cell spreading, focal adhesion formation, and actin stress fiber organization to a similar extent as fibronectin. Moreover, S1-RBD stimulated tyrosine phosphorylation of the adhesion mediators FAK, Src, and paxillin; triggered Akt activation; and supported cell proliferation. Thus, the RGD sequence of S1-RBD can function as an α_v-selective integrin agonist. This study provides evidence that cell surface α_v-containing integrins can respond functionally to spike protein and raises the possibility that S1-mediated dysregulation of extracellular matrix dynamics may contribute to the pathogenesis and/or post-acute sequelae of SARS-CoV-2 infection.

Coronaviruses (CoVs) are a diverse group of positive-stranded RNA viruses named for the distinctive crown-like protrusions on their surfaces. CoVs can infect a wide range of mammalian and avian species, causing mild to severe respiratory infections (1). At present, seven different CoVs are known to infect humans, four of which cause only mild disease (2). Within the past 20 years, three CoVs have emerged that are capable of causing more severe disease in humans: SARS-CoV-1, the cause of severe acute respiratory syndrome (SARS); MERS-CoV, the cause of Middle East respiratory syndrome (MERS); and SARS-CoV-2, the cause of COVID-19 (1). The most common symptoms of COVID-19 infection are fever, cough, shortness of breath, and fatigue (3), but disease progression varies widely with approximately 20% of non-vaccinated patients experiencing severe acute disease (4). Acute respiratory distress syndrome (5), as well as myocardial (6), renal (7), hepatic (8),and digestive (9) complications have all been reported. In addition, over half of patients with COVID-19, including those with mild, acute symptoms, exhibit a range of short and long-term post-acute sequelae that include pulmonary abnormalities, functional mobility impairment, fatigue, and joint pain (10, 11). The complex clinical manifestations of acute and post-acute COVID-19 suggest a dysregulated host response to infection that triggers immunoinflammatory, thrombotic, and parenchymal disorders (12), Yet, the pathophysiological mechanisms responsible for the diverse disease phenotypes remain largely unknown.

The extracellular matrix (ECM) glycoprotein, fibronectin, is an essential regulator of connective tissue homeostasis (13), epithelial morphogenesis (14), endothelial barrier maintenance (15, 16), local arteriolar tone (17, 18), and tissue repair (19). Fibronectin also serves a significant role in host–pathogen interactions, as fibronectin-binding and fibronectin-mimicking proteins have been identified across a broad spectrum of microbial pathogens (20). Compared with SARS-CoV-1, the spike (S)1 subunit of SARS-CoV-2 contains a novel mutation that mimics a bioactive sequence in fibronectin: a Lys (K) to Arg (R) mutation in the receptor-binding domain (RBD), resulting in the adhesive Arg-Gly-Asp (RGD) motif of fibronectin's integrin-binding domain (21). In fibronectin, the RGD sequence is located in a short loop that extends from the tenth type III repeat (FNIII10) where it mediates adhesion for a variety of cell types, including epithelial cells, endothelial cells, and fibroblasts, *via* β_1 and β_3 integrins (22, 23). Ligation of cell surface integrins with the RGD sequence of fibronectin triggers a cascade of cell signaling events, including protein kinase C activation and Rho-mediated actomyosin contractility, that lead to changes in cell shape (24), focal adhesion composition (25, 26), and extracellular matrix assembly (27). Critically,

* For correspondence: Denise C. Hocking, denise_hocking@urmc.rochester.edu.

activation of components of these adhesion-based signaling cascades has been associated with reduced endothelial and epithelial barrier function and increased prevalence of inflammatory diseases (28).

SARS-CoV-2 infects epithelial cells of both the respiratory (29) and gastrointestinal tracts (30) *via* S1-mediated recognition of angiotensin-converting enzyme 2 (ACE2) on host cell surfaces (31). Initial evaluation of interresidue distances within the crystal structure of SARS-CoV-2 spike in complex with ACE2 suggested that the RGD motif of S1 is located adjacent to, but not included within, the ACE2-binding surface (32). More recent analysis indicates that Arg403 of S1 is highly conserved across SARS-CoV-2 lineages and may facilitate viral engagement of human cells *via* an ionic interaction with residue Glu37 of ACE2 (33). Positive detection of S1-integrin binding *via* solid-phase ELISA assays has been reported by several independent groups for both $\alpha_5\beta_1$ (34, 35) and $\alpha_v\beta_3$ (36) integrins. Viral infection studies further showed that cell-surface binding and viral uptake of SARS-CoV-2 can be inhibited by integrin antagonists, including the peptide inhibitors Cilengitide (36) and ATN-161 (34, 37), as well as by cell-permeable inhibitors of inside-out integrin signaling (38). Thus, converging evidence suggests that S1-integrin interactions occur during SARS-CoV-2 infection, although the specificity and selectivity for specific integrins, as well as the implications for SARS-CoV-2 infection and disease remain to be elucidated. In the present study, we investigated S1-integrin interactions using both primary human small airway epithelial cells, as well as fibronectin-null mouse embryonic fibroblasts (FN-null MEFs). FN-null MEFs do not produce fibronectin, laminin, or vitronectin (39, 40) and are cultured in the absence of serum, allowing for the characterization of S1 binding to cell surface receptors and the identification of intracellular signals triggered by S1-integrin engagement without interference from other adhesive ligands (40–42). Results of this study indicate that the RGD motif contained within S1 is a cryptic, low-affinity, α_v integrin ligand that can mediate cell adhesion, spreading, and proliferation to a similar extent as native fibronectin. RBD-integrin engagement triggers canonical integrin-mediated signaling cascades, focal adhesion formation, and actin cytoskeletal organization, thus functioning as a classical α_v integrin agonist.

Results

S1-RBD of SARS-CoV2 supports cell adhesion and proliferation via $\alpha_v\beta_3$ integrins

The integrin-binding RGD motif is contained within a variety of endogenous ECM glycoproteins (43) and is frequently expressed by microbial pathogens as a mechanism for attachment to host tissue (44). To begin to determine whether S1-RBD functionally interacts with cells, FN-null MEFs were seeded into wells coated with either S1-RBD or the RGD-containing module of fibronectin, FNIII10. At 4 h after seeding, cells adherent to S1-RBD exhibited robust adhesion and classical fibroblast morphology, characterized by extended membrane protrusions (Fig. 1*A*). Cell adhesion was dose dependent with respect to substrate coating concentration and comparable with adhesion on FNIII10 (Fig. 1*B*). Under these assay conditions, full-length S1 supported minimal cell attachment compared with the similarly sized fibronectin fragment, FNIII8-13 (Fig. 1*C*).

Ligation of integrins by RGD-containing agonists initiates cell signaling cascades that support cell proliferation (45). Thus, we next tested the ability of S1-RBD to support cell proliferation. To do so, FN-null MEFs were seeded at low density in defined, serum-free media onto tissue culture plates coated with S1-RBD, FNIII10, or the nonadhesive, protein purification tag, glutathione S-transferase (GST). After a 4-day incubation, relative cell number was quantified as a function of coating concentration. As shown in Figure 1*D*, cell number increased similarly with increasing coating density on S1-RBD- and FNIII10-coated wells. In contrast, cells seeded into GST-coated wells did not survive (Fig. 1*D*; 1 μM), indicating that cell proliferation in response to S1-RBD was specific and not due to the presence of endogenous or exogenously supplied adhesive proteins.

Integrins are heterodimeric receptors, whose ligand specificity is determined by the combination of alpha and beta subunits (43). FN-null MEFs express α_1, α_5, α_v, β_1, and β_3 integrin subunits (40), of which both $\alpha_5\beta_1$ and $\alpha_v\beta_3$ are RGD-binding integrins (43). To identify the integrin receptors mediating cell adhesion to S1-RBD, FN-null MEFs were pre-incubated with blocking antibodies directed against β_1, β_3, α_5, or α_v integrin subunits. Cell adhesion to S1-RBD was inhibited partially by antibodies against β_3-integrin subunits and inhibited completely by either a combination of α_v- and β_3-blocking antibodies or EDTA (Fig. 2*A*). Similar results were obtained using the $\alpha_v\beta_3$-specific ligand, FNIII10 (46) (Fig. 2*B*). In contrast, cell adhesion to S1-RBD was not inhibited by either α_5- or β_1-blocking antibodies (Fig. 2*A*) under conditions that specifically inhibited adhesion to the β_1-integrin ligand, collagen I (Fig. 2*C*). Rather, treatment of cells with anti-β_1 antibodies significantly increased cell adhesion to S1-RBD (Fig. 2*A*). Finally, competitive inhibition assays were performed using short RGD-, RAD-, or KGD-containing peptides. Addition of soluble RGD peptides blocked cell adhesion to S1-RBD (Fig. 2*D*). In contrast, addition of control, RAD peptides had no effect on cell adhesion to S1-RBD (Fig. 2*D*). Furthermore, peptides derived from the RGD-containing region of SARS-CoV-2 partially inhibited cell adhesion to S1-RBD, whereas a peptide derived from the corresponding sequence of SARS-CoV-1, which contains a KGD rather than RGD motif, did not reduce adhesion to S1-RBD (Fig. 2*D*). Notably, SARS-CoV-2-derived peptides also partially inhibited cell adhesion to FNIII10 (Fig. 2*E*). Together, these data indicate that the RGD motif of S1-RBD ligates $\alpha_v\beta_3$ integrins in a cation-dependent manner.

Surface plasmon resonance (SPR) was used next to study the kinetic parameters governing the binding of recombinant human integrins with immobilized S1-RBD. Representative response curves obtained from $\alpha_v\beta_3$, $\alpha_v\beta_6$, or $\alpha_5\beta_1$ integrin binding to S1-RBD, FNIII10, or FNIII8-10 are shown in Figure 3. Experimental data were collected and globally fit

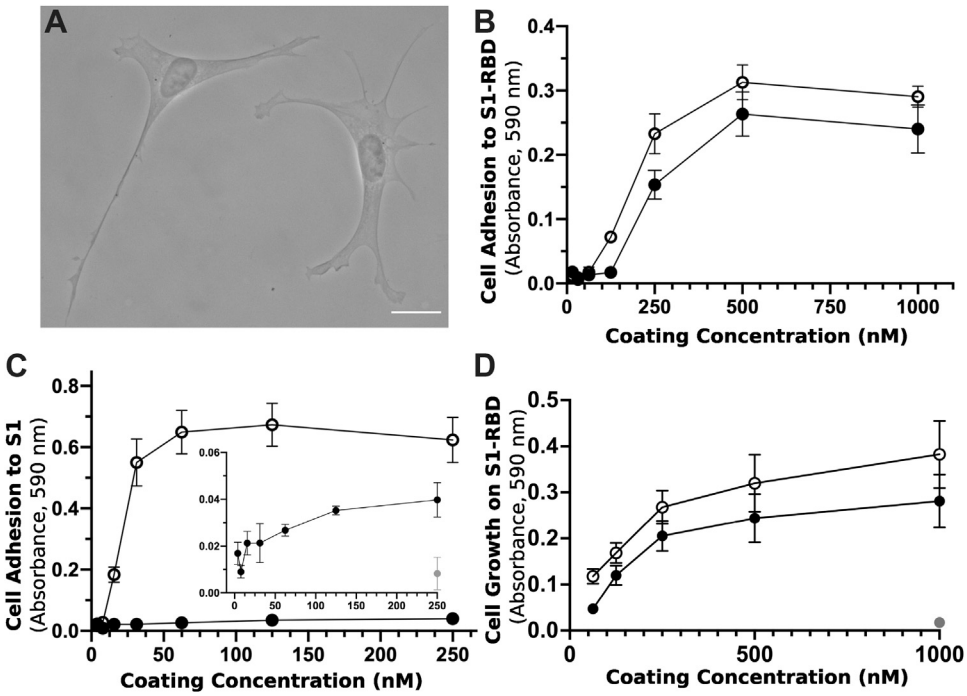

Figure 1. S1-RBD supports cell adhesion and proliferation. *A*, FN-null MEFs (2.5×10^3 cells/cm^2) were seeded onto coverslips precoated with S1-RBD (500 nM) and cultured for 4 h prior to fixation and phase-contrast imaging. The scale bar represents 20 μm. *B*, FN-null MEFs (1.9×10^5 cells/cm^2) were seeded onto tissue culture plates precoated with the indicated concentration of S1-RBD (*filled circles*) or FNIII10 (*open circles*). Cells were cultured for 90 min, and relative cell number was determined by *crystal violet* staining. *C*, FN-null MEFs (1.9×10^5 cells/cm^2) were seeded onto plates precoated with HN-tagged S1 (*filled circles*) or FNIII8-13 (*open circles*) for 90 min. Inset shows cell adhesion to S1 (*filled circles*) compared with bovine serum albumin–coated wells (*gray circle*). *D*, FN-null MEFs (2.3×10^3 cells/cm^2) were seeded onto tissue culture plates precoated with the indicated concentration of S1-RBD (*filled circles*), FNIII10 (*open circles*), or GST (*gray circle*) and cultured for 4 days. Relative cell number was determined by *crystal violet* staining. Data are mean ± SEM; n ≥ 3 experiments performed in triplicate.

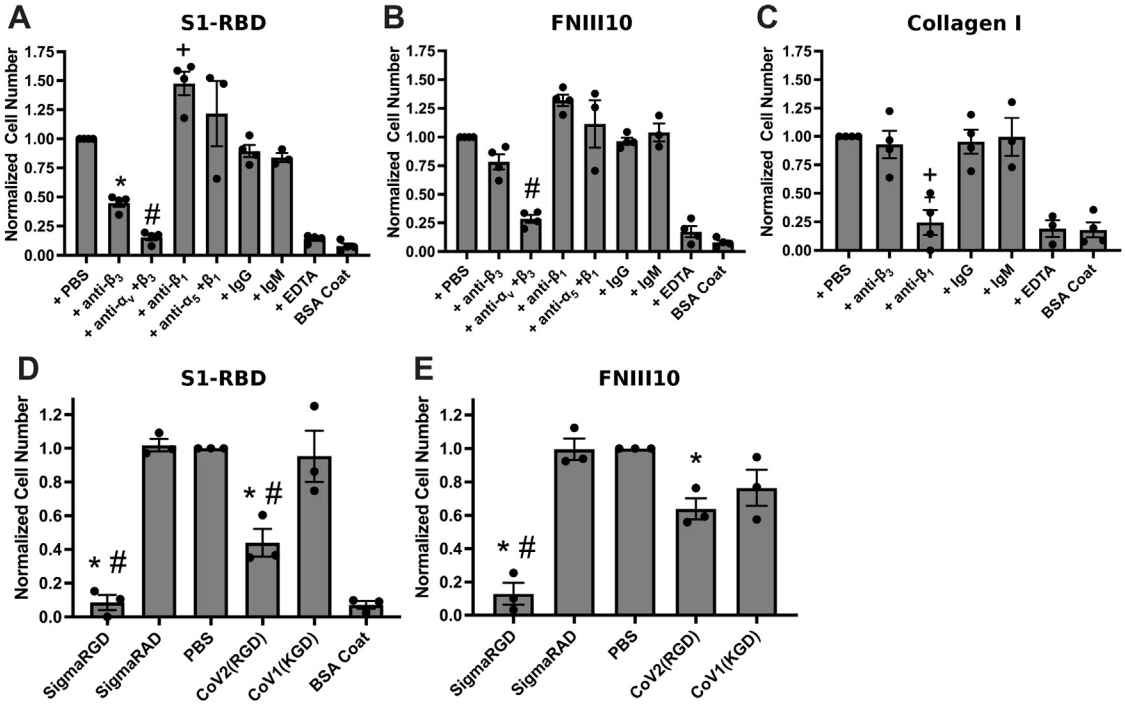

Figure 2. FN-null MEF adhesion to S1-RBD is mediated by $\alpha_v\beta_3$ integrins and RGD. FN-null MEFs (5×10^5 cells/ml) were preincubated for 30 min with 50 μg/ml integrin-blocking antibodies (*A–C*) or 25 μM peptide (*D–E*) before seeding (9.4×10^4 cells/cm^2) onto plates precoated with 250 nM S1-RBD (*A* and *D*), FNIII10 (*B* and *E*), or type I collagen (*C*). Relative cell number was determined by *crystal violet* staining. Data are mean ± SEM, normalized to corresponding vehicle (PBS) controls; n = 3 independent experiments performed in triplicate. One-way ANOVA, Bonferroni's post hoc test: *A–C* *$p < 0.05$ *versus* PBS, IgG; +$p < 0.05$ *versus* PBS, IgM; #$p < 0.05$ *versus* PBS, anti-α_5+β_1; *D–E* *$p < 0.05$ *versus* PBS; #$p < 0.05$ *versus* corresponding negative control, RAD or KGD.

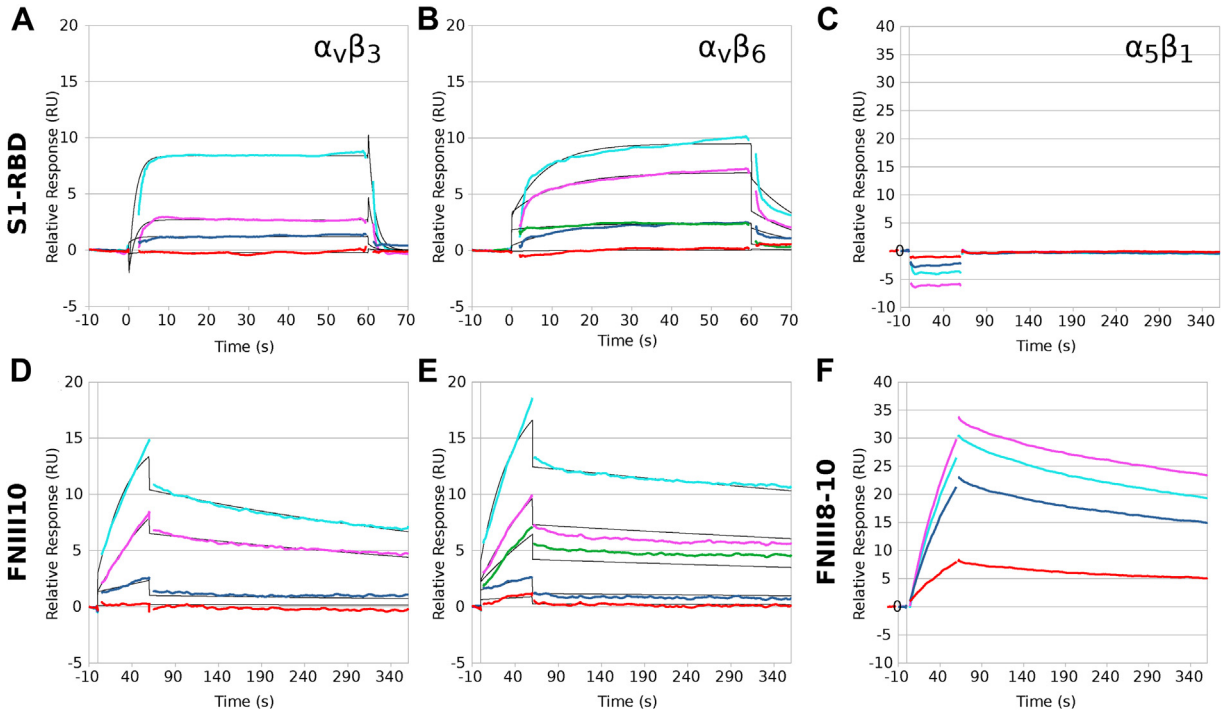

Figure 3. Recombinant human integrins $\alpha_v\beta_3$ and $\alpha_v\beta_6$, but not $\alpha_5\beta_1$, bind to immobilized S1-RBD. Representative kinetic data for $\alpha_v\beta_3$ (*A* and *D*), $\alpha_v\beta_6$ (*B* and *E*), or $\alpha_5\beta_1$ (*C* and *F*) binding to immobilized S1-RBD (*A–C*), FNIII10 (*D–E*), or FNIII8-10 (*F*). Data are presented as representative traces (*bold colored lines*) collected from one of two ($\alpha_5\beta_1$, 100–1000 nM) or three ($\alpha_v\beta_3$, 5–450 nM and $\alpha_v\beta_6$, 5–500 nM) experiments and corresponding 1:1 binding fits (*black lines*).

using a 1:1 binding model. The fitted kinetic parameters, k_a, k_d, K_D, and Rmax are shown in Table 1. The quality of each fit was evaluated by comparison with the experimentally measured Rmax and chi-squared values. Measurable binding of $\alpha_v\beta_3$ integrins to S1-RBD was observed (Fig. 3*A*). However, curve-fitting parameters indicated that the goodness of fit was not sufficient to perform kinetic analysis, suggesting that the K_D of $\alpha_v\beta_3$ integrins binding to S1-RBD is greater than 500 nM (Table 1). Kinetic modeling of data obtained for $\alpha_v\beta_6$ integrin binding to S1-RBD provided a K_D value of 230 nM (Fig. 3*B* and Table 1). In contrast, $\alpha_5\beta_1$ integrins did not bind to S1-RBD (Fig. 3*C*), in agreement with results of cell adhesion assays (Fig. 2). Measured affinities of FNIII10 binding to $\alpha_v\beta_3$ (Fig. 3*D*) and $\alpha_v\beta_6$ (Fig. 3*E*) integrins were 21.8 nM and 6.6 nM, respectively (Table 1), which are similar to published values (47). Association rates for the interaction of $\alpha_v\beta_6$ integrins with S1-RBD and FNIII10 were similar (S1-RBD k_a = 8.4×10^4 $M^{-1}s^{-1}$; FNIII10 k_a = 7.1×10^4 $M^{-1}s^{-1}$). In contrast, the dissociation rate of $\alpha_v\beta_6$ integrins with S1-RBD was much larger than that observed with FNIII10 (S1-RBD k_d = 236×10^{-4} s^{-1}; FNIII10 k_d = 6.0×10^{-4} s^{-1}). Kinetic fits were not performed for the reaction of S1-RBD and $\alpha_5\beta_1$ integrins, as binding was not observed (Fig. 3*C*) even at analyte concentrations substantially exceeding the K_D of the interaction of FNIII8-10 with $\alpha_5\beta_1$ integrins (47) and under reaction conditions in which $\alpha_5\beta_1$ integrin binding to FNIII8-10 was observed (Fig. 3*F*). Together, these data indicate that S1-RBD is capable of binding directly to α_v integrins through low-affinity interactions.

S1-RBD initiates focal adhesion formation and actin organization

Integrin ligation by endogenous ECM ligands triggers adhesion signaling cascades in which intracellular mediators are recruited to sites of integrin activation (45, 48). These protein complexes, known as focal adhesions, serve as central signaling hubs and functionally couple ECM-engaged integrins to the actin cytoskeleton (49). Notably, manipulation of focal adhesion signaling has been identified across a diverse spectrum of microbial pathogens, with the potential to influence multiple stages of cellular pathophysiology, including cell-

Table 1
Summary of kinetic and quality control parameters determined for the interaction of α_v integrins with immobilized S1-RBD and FNIII10

Ligand	Analyte	$k_a \times 10^4$	$k_d \times 10^{-4}$	K_D (nM)	Rmax fit (RU)	Rmax measured (RU)	Chi^2
S1-RBD	$\alpha_v\beta_3$	-	-	>500	-	-	-
S1-RBD	$\alpha_v\beta_6$	8.4 ± 1.8	236 ± 206	230 ± 180	6.9 ± 3.5	11.7 ± 0.7	0.1 ± 0.3
FNIII10	$\alpha_v\beta_3$	7.1 ± 1.4	15.0 ± 1.8	21.8 ± 1.6	12.8 ± 0.5	12.6 ± 0.4	0.06 ± 0.01
FNIII10	$\alpha_v\beta_6$	25.0 ± 18.8	6.0 ± 0.7	6.6 ± 3.1	16.6 ± 2.5	19.0 ± 2.3	0.16 ± 0.05

Data are presented as mean ± SEM for at least three independent experiments per integrin. Double-referenced experiments were performed simultaneously for S1-RBD and FNIII10 ligands in parallel flow cells.

surface attachment, invasion, and cell death (44). To determine whether engagement of $\alpha_v\beta_3$ integrins by S1-RBD supports focal adhesion formation and downstream signaling, FN-null MEFs adherent to S1-RBD were stained with the actin-binding protein phalloidin, together with antibodies against the focal adhesion adaptor vinculin, and a pan-specific phosphotyrosine antibody (50). Cells adherent to S1-RBD- or FNIII10-coated substrates were well spread and exhibited classical features of focal adhesions, including colocalized vinculin and phosphotyrosine staining, as well as actin stress fiber formation (Fig. 4). S1-RBD-adherent cells typically exhibited fewer, but larger, focal contacts than FNIII10-adherent cells.

To identify proteins specifically phosphorylated by S1-RBD ligation, immunoblot analysis of whole-cell lysates was performed. Similar patterns of protein tyrosine phosphorylation were observed when lysates from attached S1-RBD- or FNIII10-adherent cells were probed with a pan-specific phosphotyrosine antibody (not shown). As such, immunoblots were next probed with phosphospecific antibodies against key components of adhesion signaling pathways (Fig. 5). These components included the early, adhesion-dependent autophosphorylation of focal adhesion kinase (FAK) at Y^{397} (51), which in turn enables recruitment and phosphorylation of Src at Y^{418} (52). Both FAK-Y^{397} and Src-Y^{418} were phosphorylated in response to S1-RBD ligation (Fig. 5). Moreover, the extent of FAK and Src phosphorylation was similar to that observed in either FNIII-10- or fibronectin-adherent cells (Fig. 5). FAK may be phosphorylated at additional tyrosine residues including Y^{407} (53), which was phosphorylated to a similar extent in both suspended and adherent cells (Fig. 5). S1-RBD triggered tyrosine phosphorylation of paxillin (Fig. 5), a central adaptor protein whose SH2 domains require phosphorylation at residues Y^{118} and Y^{31} for activation and cytoskeletal remodeling (54, 55). In addition, S1-RBD induced Akt phosphorylation at residue S^{473} to a similar extent as FNIII10- and fibronectin-adherent cells, implicating engagement of the prosurvival PI3K/Akt signaling axis (56, 57) and consistent with results demonstrating that S1-RBD ligation supports cell proliferation (Fig. 1*D*). Together, these data indicate that S1-RBD can trigger multiple aspects of adhesion-based signaling, including localization of vinculin to focal adhesions, phosphorylation of early adhesion signals FAK and Src, as well as activation of downstream adhesive effectors, including paxillin and Akt.

The data presented thus far indicate that the RGD sequence within S1-RBD is a functional, integrin-binding ligand that can mimic classical features and functions of native ECM ligands. In contrast, cells attached poorly to a larger fragment of S1 (Fig. 1*C*), which contains both the N-terminal domain and furin cleavage site in addition to RBD. Cryptic adhesive epitopes are a feature common to many native ECM proteins, including fibronectin (58) and thrombospondin (59). Thus, studies were conducted to explore conditions that might

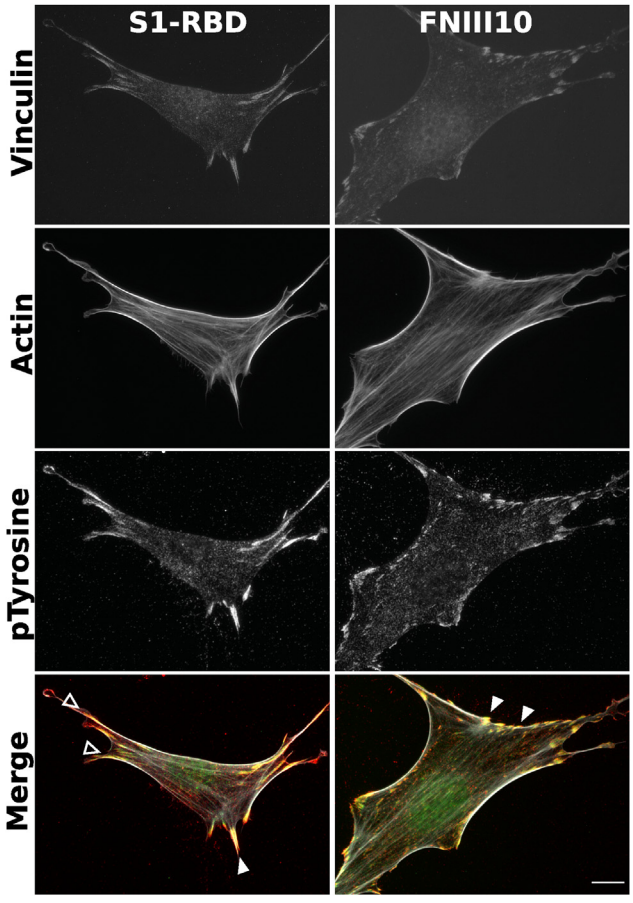

Figure 4. S1-RBD engagement initiates focal adhesion formation and actin organization. FN-null MEFs (2.5×10^3 cells/cm^2) were seeded on coverslips coated with 500 nM S1-RBD (*left*) or FNIII10 (*right*). Cells were incubated for 4 h prior to fixation and immunofluorescent staining for vinculin (*green*), actin (TRITC-phalloidin, *white*), or phosphotyrosine (4G10, *red*). *Arrowheads* represent colocalization of vinculin and phosphotyrosine within focal adhesions (closed) and engagement with the actin cytoskeleton (open). Representative images shown from one of four independent experiments. The scale bar represents 10 μm.

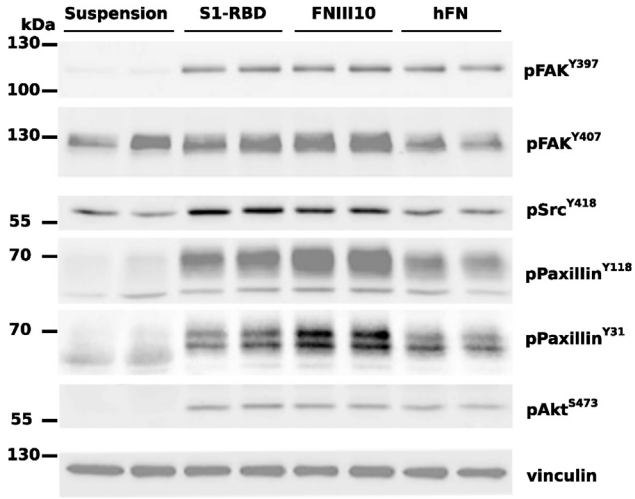

Figure 5. Cell engagement with S1-RBD stimulates intracellular signaling. FN-null MEFs were either suspended in media or seeded at 3.5×10^5 cells/cm^2 on wells precoated with 500 nM of S1-RBD or FNIII10, or 10 μg/ml of human plasma fibronectin (hFN) for 1 h. Cell lysates were analyzed by immunoblotting with the indicated phosphospecific antibodies or vinculin, as a loading control. Molecular mass markers are shown on the *left*.

promote cell interactions with the larger S1 fragment. First, S1 was chemically reduced to alter its conformation. Cell adhesion to substrates precoated with either reduced or nonreduced S1 was then determined in the absence and presence of $MnCl_2$, a potent activator of $\alpha_v\beta_3$ integrins (60). In the absence of $MnCl_2$, few cells attached to S1, either in the nonreduced or reduced form (Fig. 6*A*, S1 - $MnCl_2$). In contrast, in the presence of $MnCl_2$, cells were visibly attached and well spread on substrates coated with either nonreduced or reduced S1, compared with bovine serum albumin (BSA)-coated wells (Fig. 6*A*, S1 + $MnCl_2$). Cells attached and spread similarly on S1-RBD-coated substrates in the absence and presence of $MnCl_2$ (Fig. 6*A*, S1-RBD ± $MnCl_2$) indicating that integrin interaction with RBD did not require the high-affinity state.

Cell attachment to S1 was quantified using adhesion assays. In the presence of $MnCl_2$, cell attachment to wells coated with reduced S1 was statistically increased *versus* BSA-coated wells (Fig. 6*B*; reduced S1 + $MnCl_2$ *versus* BSA + $MnCl_2$). Moreover, adhesion to reduced S1 was sensitive to the metal ion chelator, EDTA (Fig. 6*B*, reduced S1 ± EDTA). To determine whether increased cell adhesion to reduced S1 was due to changes in S1 protein conformation or increased substrate coating efficiency, ELISAs were performed on substrate-coated wells using anti-His antibodies. The relative coating density of reduced S1 was approximately double that of nonreduced S1 and S1-RBD (mean absorbances ± SD: reduced S1 = 1.56 ± 0.04; nonreduced S1 = 0.76 ± 0.01; S1-RBD = 0.95 ± 0.08). As such, the increase in cell adhesion observed with reduced S1 protein was likely due to an increase in coating density of the reduced S1 protein. There was no significant difference in protein density of wells coated with nonreduced S1 *versus* RBD. Together, these data indicate that, within the larger S1 fragment, the adhesive capacity of RBD is detectable but substantially reduced *versus* the RBD fragment.

S1-RBD exhibits cation- and RGD-dependent binding to primary human small airway epithelial cell monolayers

We next sought to determine whether S1-RBD can mediate adhesion of human primary small airway epithelial cells (hSAECs). These primary cells are derived from the distal lung and are susceptible to SARS-CoV-2 infection (61, 62). hSAECs seeded in the presence of 1 mM $MnCl_2$ attached and spread on S1-RBD-coated wells to a similar extent as that observed with laminin-coated wells (Fig. 7, *A* and *B*). hSAEC adhesion to S1-RBD was significantly increased compared with BSA-coated wells and was similar to that observed with wells coated with the αvβ3-ligand, FNIII10 (Fig. 7*C*). Furthermore, hSAECs adhesion to S1-RBD stimulated tyrosine phosphorylation of FAK, paxillin, and Src to a similar extent as FNIII10 and fibronectin (Fig. 7*D*). Thus, S1-RBD stimulates adhesion-

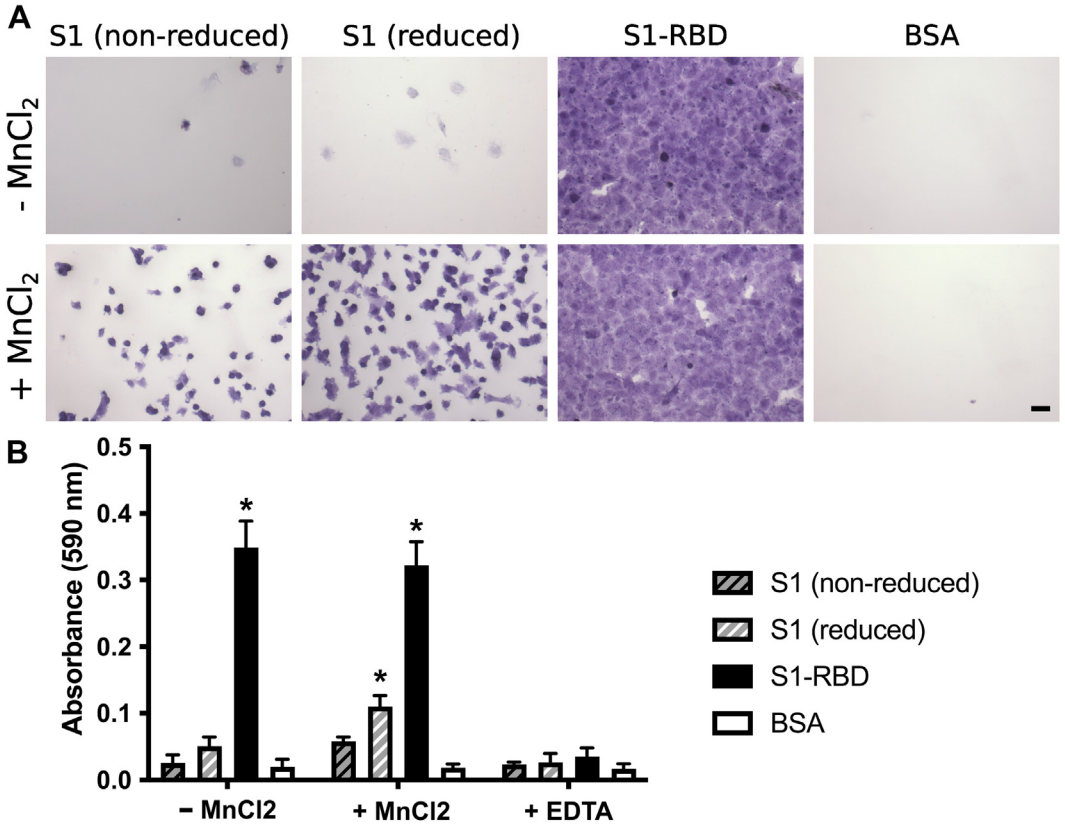

Figure 6. S1 contains a cryptic, Mn^{2+}-sensitive adhesive epitope. *A*, FN-null MEFs (9.4×10^4 cells/cm^2) were seeded on wells precoated with 250 nM reduced or nonreduced S1 protein, S1-RBD, or 1% bovine serum albumin (BSA). Cells were seeded for 1 h in the absence or presence of 1 mM $MnCl_2$ or 10 mM EDTA. *A*, representative images of *crystal violet*–stained cells. The scale bar represents 100 μm. *B*, relative cell number presented as mean absorbance ± SEM, n = 3 independent experiments performed in triplicate. *$p < 0.05$ *versus* corresponding BSA control by two-way ANOVA with Bonferroni's post hoc test.

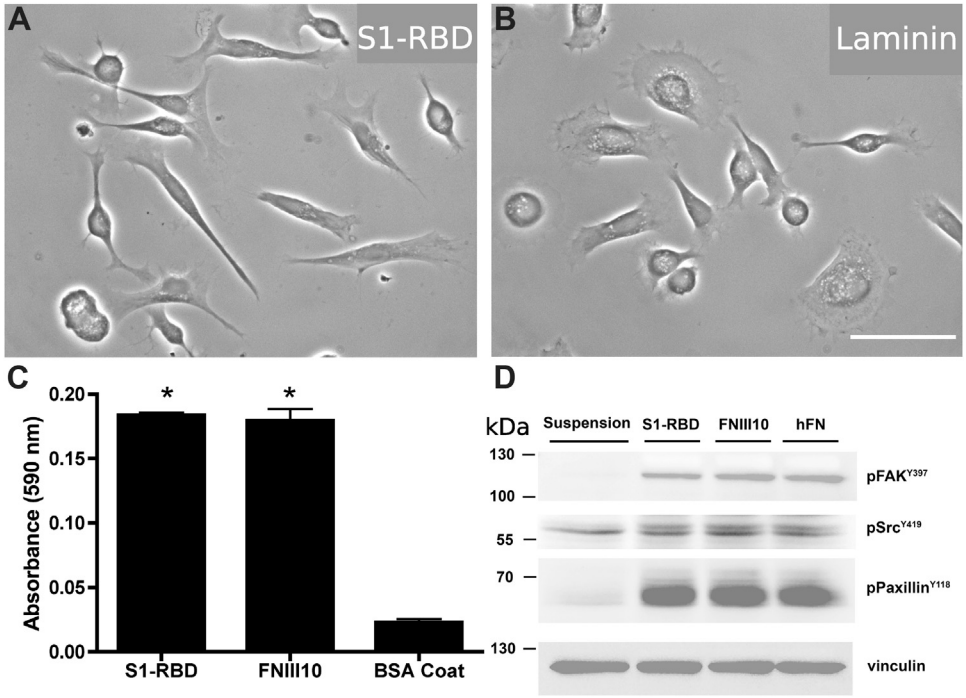

Figure 7. S1-RBD supports cell adhesion and phosphotyrosine signaling in human small airway epithelial cells. hSAECs (6.7×10^4 cells/cm^2) were seeded in the presence of 1 mM $MnCl_2$ on wells precoated with S1-RBD, laminin, FNIII10, or 1% bovine serum albumin (BSA). Representative images of SAECs adherent of S1-RBD (*A*) or laminin (*B*) are shown. The scale bar represents 50 μm. *C*, cell adhesion after 2 h was determined by *crystal violet* staining. Data are presented as mean absorbance ± SEM. *$p < 0.05$ *versus* BSA by one-way ANOVA with Bonferroni's posttest. *D*, cell lysates were obtained after 4 h of adhesion and analyzed by immunoblotting with the indicated phosphospecific antibodies. Vinculin was used as a loading control. Molecular mass markers are shown on the *left*. Control cells were maintained suspended in medium before lysing. SAEC, small airway epithelial cell.

mediated intracellular signaling pathways in human lung epithelial cells.

Thus far, the ability of S1-RBD to bind to integrins has been analyzed by presenting immobilized S1 fragments to non-adherent cells. To evaluate S1-RBD binding to cells that are already adherent and spread on native ECM substrates, assays were performed using either Fc-tagged RBD fragments immobilized on fluorescent protein G–coupled microbeads or biotin-tagged CoV 20-mer peptides immobilized on streptavidin-coupled microbeads. To begin, hSAEC monolayers were incubated with RBD- or IgG-immobilized beads. Following a 2-h incubation, limited binding of IgG-coupled beads to hSAEC monolayers was observed (Fig. 8*A*; IgG + MnCl2). In contrast, RBD-immobilized beads attached extensively to hSAECs in the presence but not the absence of $MnCl_2$ (Fig. 8*A*). Quantification of the number of beads bound per imaging field indicated a significant increase in the number of RBD-beads bound *versus* IgG controls (Fig. 8*B*), demonstrating cation-dependent binding of S1-RBD to epithelial cell surfaces.

The role of the RGD motif in mediating RBD binding to epithelial cell surfaces was next assessed using CoV-derived peptides. A 20-mer, CoV-2 peptide encompassing the RGD motif was synthesized, and binding to epithelial cell surfaces was compared with the corresponding peptide of CoV-1, which contains a KGD sequence in place of RGD. The CoV-1 sequence was chosen expressly as a control for CoV-2 binding, as KGD is also an integrin-binding motif but with specificity for platelet αIIbβ3 integrins (63), which are not expressed by primary epithelial cells (64). Peptide-bound microbeads were incubated with laminin-adherent SAECs for 2 h, and unbound beads were removed by washing. As shown in Figure 8*C*, microbeads coated with RGD-containing CoV-2 peptides readily attached to epithelial cell surfaces, whereas beads coated with KGD-containing CoV-1 peptides did not. Quantification of the number of beads bound per imaging field indicated a significant increase in the number of CoV-2- *versus* CoV-1-beads bound per region of interest (Fig. 8*D*). The CoV-1- and CoV-2-derived peptides utilized in this study differ only in their integrin-binding sequences (IRGDE *versus* VKGDD for CoV-2 and CoV-1, respectively), thus providing additional evidence that mutation of the KGD sequence of CoV-1 to RGD conferred the RBD of CoV-2 with the capacity to interact with epithelial cell integrins.

Discussion

The identification of a conserved RGD motif within the SARS-CoV-2 spike protein generated substantial scientific interest (21, 33), and converging lines of experimental evidence suggest that integrin inhibition may be protective against SARS-CoV-2 binding and infection (34, 36–38, 65). To the best of our knowledge, the data presented in the present study are the first to demonstrate that the receptor-binding domain of SARS-CoV-2 spike protein functions as a classical integrin receptor agonist. S1-RBD supported cell adhesion (Fig. 1, *A* and *B*) and proliferation (Fig. 1*D*) to comparable extents as the RGD-containing fragment of the native ECM molecule fibronectin (FNIII10). This interaction was

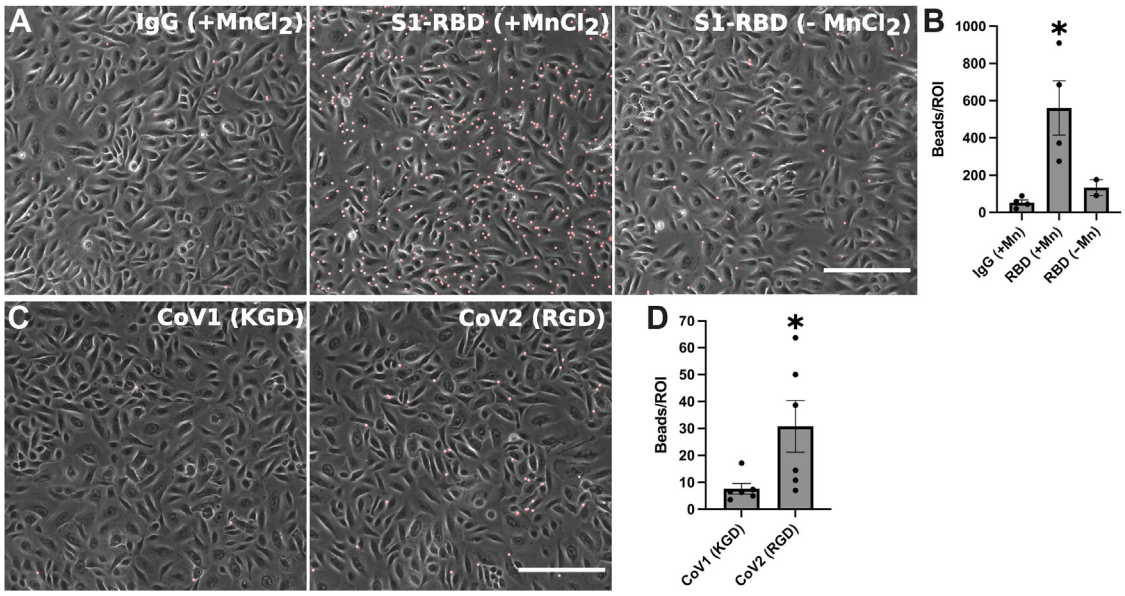

Figure 8. S1-RBD-bound beads bind to SAEC monolayers in a cation- and RGD-dependent manner. *A*, laminin-adherent SAEC monolayers were treated with (*A* and *B*) IgG- or Fc-RBD-immobilized fluorescent microbeads in the presence or absence of 1 mM $MnCl_2$ or (*C* and *D*) biotinylated CoV-2(RGD) or CoV-1(KGD) peptide-immobilized fluorescent microbeads in the presence of 1 mM $MnCl_2$. Cells were incubated for 2 h at 4 °C. (*A* and *C*) representative phase images are shown; protein-immobilized beads are *red*. The scale bar represents 200 μm. (*B* and *D*) bead binding to SAEC monolayers was quantified as the mean for three independent regions of interest (ROIs) per well. Data are mean number of beads bound per 0.6 mm^2 ROI ± SEM. In (*B*), n = 4 (+Mn) or n = 2 (−Mn) replicates per condition on two independent experimental days. *$p < 0.05$ *versus* IgG by one-way ANOVA with Bonferroni's post hoc test. In (*D*), n = 6 replicates per condition on three independent experimental days. *$p < 0.05$ *versus* KGD by two-tailed *t* test. SAEC, small airway epithelial cell.

competitively inhibited by both α_v integrin-blocking antibodies and RGD peptides (Fig. 2, *A* and *D*) and was also observed in an SPR model of direct S1-RBD-integrin binding (Fig. 3). Cells adherent to S1-RBD formed focal adhesions (Fig. 4), and key adhesion signaling mediators FAK, Src, Paxillin, and Akt were phosphorylated (Fig. 5). The present studies were conducted primarily in mouse embryonic fibroblasts, which do not express detectable levels of ACE2, and thus these results are unlikely to be complicated by potential interactions of S1-RBD with ACE2. As well, S1-RBD supported both cell attachment and adhesion-based signaling in primary human small airway epithelial cells (Fig. 7), while RBD-bound microbeads attached readily to SAEC monolayers (Fig. 8). Together, these results demonstrate that SARS-CoV-2 spike protein contains a functional adhesive epitope within the RBD that mediates α_v integrin engagement *via* its RGD motif.

Of reports investigating integrin-spike interactions, $\alpha_5\beta_1$ has been proposed as a receptor of interest, in part due to its functional association with ACE2 (66, 67), the ability of β1-selective integrin antagonists to reduce SARS-Co-V2 invasion (34, 37, 38), and observed $\alpha_5\beta_1$ integrin-S1-RBD interactions by ELISA (34) and SPR (68) assays. Some reports have also implicated $\alpha_v\beta_3$ integrins in viral entry (36, 69), while others found no effects of integrin antagonists on viral invasion (33). In the present study, we compared effects of β_1- and β_3-integrin-blocking antibodies on cell attachment to RBD using a well-characterized fibroblast cell line that expresses both functional $\alpha_5\beta_1$ and $\alpha_v\beta_3$ integrin receptors (40, 41). Notably, FN-null MEFs do not produce fibronectin, are cultured in the absence of serum, and do not deposit other endogenous matrix molecules, including RGD-containing thrombospondin and the $\alpha_{1/2}\beta_1$ integrin ligand collagen, into their ECM (42). FN-null MEFs adhered to S1-RBD exclusively *via* $\alpha_v\beta_3$ integrins, with no contribution from $\alpha_5\beta_1$ integrins (Fig. 2, *A*–*C*). This result was confirmed using recombinant integrins and SPR, which further indicated that the affinity of the epithelial integrin $\alpha_v\beta_6$ for S1-RBD was substantially higher than that of $\alpha_v\beta_3$ (Fig. 3 and Table 1). In contrast to previous reports (68), we found no detectable interaction between S1-RBD and $\alpha_5\beta_1$ integrin using SPR. This intriguing finding may be due to differences in the SPR conditions, which in the present study, included the use of the nonionic detergent octyl glucoside (70) and $MnCl_2$ (60, 71) to support functional activation of integrins within a purified protein system. While we did not test the integrin specificity of the larger S1 fragment in the present study, recent work by Park and colleagues (65) showed that an Fc-tagged S1 fragment could support α_v-, α_4-, or β_1-mediated adhesion depending on cell type–specific integrin expression. Thus, the possibility remains that, like fibronectin (46, 47), synergistic sequences or conformational flexibility within the larger S1 domain may confer additional, dynamic integrin selectivity. The specificity and selectivity of spike and spike fragments may further be sensitive to modulators of integrin signaling, such as heparin sulfate proteoglycan coreceptors (72) or cell-surface proteases (73), both of which have been identified as factors regulating engagement of SARS-CoV-2 virions with host target cells (31, 33, 74, 75).

In contrast to the robust adhesive response observed on S1-RBD, cells seeded onto the larger S1 fragment of SARS-CoV-2 spike protein attached only weakly and exhibited limited spreading (Figs. 1*C* and 7*B*). Cell adhesion to S1 was partially

rescued by chemical reduction of S1, which increased coating efficiency, and pretreatment of cells with Mn^{2+}. One possible interpretation of these data is that the adhesive epitope contained within S1 is cryptic and thus only available to integrins under appropriate physical and chemical conditions. This hypothesis is further supported by molecular dynamics simulations suggesting that, in the absence of other interactions, the RGD site is unable to adopt the geometry necessary for high-affinity integrin ligation (76). Matricryptic epitopes have been identified in a number of native ECM proteins, including thrombospondin (59), which contains a cryptic RGD sequence whose exposure is regulated by cell-surface protein disulfide isomerases (77). Likewise, exposure of a self-association epitope in fibronectin (58) can be exposed by cell-derived mechanical force (78) and proteolytic fragmentation (58). Thus, the specific conformational requirements and activation steps enabling functional engagement of integrin receptors with SARS-CoV-2 spike in the context of established mechanisms of viral attachment and invasion represents an open question of substantial importance.

The intact, trimeric SARS-CoV-2 spike undergoes multiple conformational changes and molecular interactions during the viral invasion process (79), including conformational flexibility of the RBD domain (80, 81), as well as activation by cell-surface proteases TMPRSS2 (31) and Cathepsin L (33, 75). Separation of the RBD from the prefusion spike trimer during proteolytic activation may therefore be a critical activation step prior to integrin binding. Furthermore, the well-characterized, cell-surface spike receptor ACE2 (31, 33) and the more recently identified coreceptor heparin sulfate proteoglycans (74, 82) can associate laterally with integrins on human cell surfaces (66, 67, 83, 84). Thus, integrins and associated intracellular signaling partners are emerging as putative components of a larger molecular complex that is targeted during SARS-CoV-2 infection. Differences in baseline integrin expression and activation state between cell lines are also a likely contributing factor in conflicting reports on the integrin dependence and selectivity of SARS-CoV-2 infection (33, 34, 36–38, 69). Future elucidation of the conformational requirements and activation steps enabling functional engagement of integrin receptors with SARS-CoV-2 spike in the context of established mechanisms of viral attachment and invasion represents an open question of substantial importance.

The demonstration of an α_v-specific integrin agonist functionality contained within S1-RBD protein opens multiple avenues that will be critical in expanding scientific understanding of SARS-CoV-2 and therapeutic options for a global population affected by the COVID-19 pandemic. The most immediate among these, the identification of anti-integrin therapeutics that are US Food and Drug Administration approved or in preclinical trials with potential efficacy against SARS-CoV-2 infection, is already underway (85). Integrins have been implicated in the pathophysiology of numerous respiratory viruses, including human cytomegalovirus (86), hantaviruses (87), and influenza (88), as either primary receptors or as major mediators of host response and disease severity, with the specific contributions of integrins in the context of COVID-19 disease yet to be elucidated (21, 89). Meanwhile, numerous questions remain unanswered regarding mechanisms underlying the differential susceptibility of vulnerable populations to severe manifestations of COVID-19 (3), as well as potential differences in infectivity, transmissibility, disease severity, and immune evasion associated with novel variants (https://covariants.org/) (90). Interrogating these open challenges in the context of integrin-spike interactions, including factors determining integrin selectivity and specificity, is a promising and yet unexplored avenue. For example, ACE2 cell surface expression levels alone do not sufficiently predict tissue susceptibility or disease severity (91). Thus, a combinatorial expression profile of ACE2, alongside α_v integrin surface expression, may better predict cell tropism of SARS-CoV-2. Alternatively, fibronectin–integrin interactions play a key role in maintaining endothelial barrier function during sepsis (15, 16, 92–95), which may be disrupted by competition from spike protein fragments during SARS-CoV-2-driven inflammation, a hypothesis that is supported by recent work in vascular endothelial cells (35). Variations in integrin expression and activation state are likewise associated with some of the key risk factors for severe complications of SARS-CoV-2 infection (3), including diabetes (96, 97), hypertension (98–100), and differing inflammatory responses (88, 101). As the global COVID-19 pandemic approaches a new, endemic stage, targeting the emerging spike-integrin signaling axis has the potential to become an essential tool in preventing or mitigating the most severe effects of the disease, particularly for vulnerable patients who are not fully protected by current preventative and therapeutic regimens.

Conclusions

The SARS-CoV-2 spike protein contains a novel RGD motif within its receptor-binding domain (S1-RBD). We demonstrate that S1-RBD is a functional integrin agonist with selectivity for α_v integrins, specifically $\alpha_v\beta_3$ and $\alpha_v\beta_6$. In contrast, we found no evidence of S1-RBD engagement with $\alpha_5\beta_1$ integrins in either cellular adhesion or SPR systems. S1-RBD-mediated cellular adhesion supported cell spreading and cytoskeletal engagement, focal adhesion formation, and stimulation of key intracellular signaling pathways associated with cytoskeletal organization and cell proliferation. Together, these data point to a functional role for α_v integrins during attachment and invasion of SARS-CoV-2 and provide insight into critical open questions regarding COVID-19 pathophysiology, including mechanisms underlying variable disease severity, intersecting risk factors, and post-acute viral sequelae.

Experimental procedures

Reagents

Fibronectin was purified from outdated human plasma (American Red Cross) using gelatin-Sepharose (GE Life

Sciences, now Cytiva) affinity chromatography (102). Type I collagen (rat tail) was purchased from Corning (354236). Unless otherwise indicated, chemicals were obtained from J.T. Baker or Sigma-Aldrich. GST-tagged FNIII10 and HN-tagged FNIII10-13 were produced and purified from *Escherichia coli* as described (46, 103). His-tagged S1 and S1-RBD of SARS-CoV-2 were purchased from Sino Biological (40591-V08H) and R&D Systems (10523-CV), respectively. Fc-tagged S1-RBD was from R&D Systems (10565-CV). Where indicated, S1 was reduced by successive 1-h treatments with 10 mM DTT and 30 mM N-ethyl maleimide (NEM) at 37 °C. Both reduced and nonreduced S1 were dialyzed into PBS prior to use. Integrin-blocking antibodies anti-α_5 (clone 5H10-27), anti-α_V (clone H9.2B8), anti-β_1 (clone Ha2/5), and anti-β_3 (clone 2C9.G2) and isotype controls were purchased from BD Biosciences. Antibodies for immunofluorescent staining were as follows: vinculin (clone VIN-11-5, Sigma or clone 42H89L44, Invitrogen); phosphotyrosine (clone 4G10, Sigma or PY20, BD Biosciences); phospho-FAK pY407 (polyclonal, Invitrogen #44650G); phospho-FAK pY397 (polyclonal, Biosource #44-624G); phospho-Src pY418 (polyclonal, Biosource #44-660); phospho-Paxillin pY118 (polyclonal, Invitrogen #44-722G); phospho-Paxillin pY31 (polyclonal, Invitrogen #44-720G); phospho-Akt pS473 (polyclonal, Cell Signaling #9271); TRITC-labeled phalloidin (Millipore, #90228). Alexa Fluor–conjugated secondary antibodies were from Molecular Probes. RGD-containing peptides derived from SARS-CoV-2 (ADSFVIRGDEVRQIAPGQTG) and KGD-containing peptides derived from SARS-CoV (ADSFVVKGDDVRQIAPGQTG) were produced with and without an N-terminal biotin-Ahx tag by Genscript. Integrin-blocking (GRGDSP, #SCP0157) and negative control (GRADSP, #SCP0156) peptides were purchased from Sigma. Recombinant human integrins αvβ3 (3050-AV), αvβ6 (3817-AV), and α5β1 (3230-A5) were from R&D Systems. Protein G–coated pink (PGFP-5058-5, 5.0–5.9 μm diameter) and streptavidin-coated Nile red (SVFP-6056-5, 5.0–7.9 μm diameter) fluorescent particles were purchased from Spherotech, Inc.

Cell culture

FN-null MEFs, derived previously from homozygous fibronectin knockout mouse embryos (40), were cultured under serum- and fibronectin-free conditions on collagen I–coated tissue culture flasks using a 1:1 mixture of Aim V (Invitrogen) and Corning SF Medium (Corning), as described (40). FN-null MEFs do not express vitronectin or laminin (39, 40) and in the absence of supplemental fibronectin are unable to assemble ECM fibrils of collagen I (104), thrombospondin (42), or fibrinogen (105). Adult human small airway epithelial cells (SAECs) were purchased from Lonza (CC-2547) and used between passages 6 and 8. SAECs were cultured in serum-free Small Airway Epithelial Growth Medium (Lonza CC-3118), according to manufacturer's instructions. Cells were passaged at 70 to 80% confluence using ReagentPack subculture reagents (Lonza CC-5034). Neither FN-null MEFs nor SAECs expressed detectable levels of ACE2 protein by immunoblot analysis (data not shown).

Cell adhesion and proliferation assays

Cell adhesion assays were performed as described (41). Briefly, 96-well tissue culture plates were coated with S1-RBD (10–1000 nM), FNIII10 (10–1000 nM), GST (1000 nM), or S1 (7.8–250 nM) for 1 h at 37 °C. Relative protein coating concentrations were quantified by enzyme-linked immunoabsorbent assays (ELISA) using anti-His antibodies, as described (106). Cells were seeded on protein-coated wells (9.4×10^4 cells/cm^2) in either AimV/SF medium (FN-null MEFs) or Small Airway Epithelial Basal Medium (CC-3119; Lonza) in the absence or presence of EDTA (10 mM), DTT (1 mM), or $MnCl_2$ (1 mM) as indicated; $MnCl_2$ was added 1 h after seeding. For integrin blocking studies, FN-null MEFs were preincubated with anti-integrin antibodies (50 μg/ml) or 25 μM peptide for 1 h prior to seeding. Integrin-blocking studies were performed using subsaturating protein coating concentrations to reduce the amount of antibody or peptide required to inhibit adhesion. Cells were then seeded into wells and incubated at 37 °C and either 8% (FN-null MEFs) or 5% (SAECs) CO_2 for up to 2 h. Wells were washed with PBS to remove nonadherent cells, fixed with 1% paraformaldehyde, and stained with 0.5% crystal violet. The absorbance of crystal violet solubilized in 1% SDS was measured at 590 nm. Proliferation assays were performed by seeding FN-null MEFs (2.5×10^3 cells/cm^2) on protein-coated 48-well plates. Cells were cultured for 4 days at 37 °C, 8% CO_2 and then fixed and stained with crystal violet (41). In some experiments, images of adherent cells were obtained after crystal violet staining and before solubilization, using an IX70 inverted microscope (Olympus) equipped with a Micropublisher 3.3 RTV digital camera (Q Imaging).

Surface plasmon resonance

Kinetic studies of integrin–ligand interactions were performed using a BIAcore T200 instrument (Cytiva). Ligands (S1-RBD or FNIII10) were immobilized using amine-coupling chemistry according to the manufacturer's instructions (BR-1000-50). Briefly, ligands diluted in 10 mM sodium acetate (pH 4.0, Cytiva) were immobilized on an EDC/NHS-activated CM5 chip (Cytiva) to a target level of 800 to 1000 RU. Excess amine-reactive groups were inactivated with 1 M ethanolamine (pH 8.5, Cytiva). Immobilization buffer was 10 mM Hepes buffer pH 7.4 containing 0.05% n-octyl-β-D-glucopyranoside (OGPS, Anatrace), 150 mM $NaCl_2$, 2 mM $MnCl_2$, 2 mM $MgCl_2$, and 0.2 mM $CaCl_2$. Lyophilized integrins were reconstituted with 50 mM Tris, pH 7.4 containing 25 mM OGPS, 1 mM DTT, 150 mM $NaCl_2$, and divalent cations (α_v integrins: 2 mM $MnCl_2$, 2 mM $MgCl_2$, and 0.5 mM $CaCl_2$; $\alpha_5\beta_1$ integrin: 2 mM $MnCl_2$). Double-referenced binding experiments were performed in parallel flow cells for S1-RBD and the corresponding positive control (FNIII10 for α_v integrins; FNIII8-10 for $\alpha_5\beta_1$) (46) using a flow rate of 30 μl/min for 1 min with a dissociation time of 5 min. Surfaces were regenerated between injections using two 30-s injections of 20 mM EDTA and 1 M NaCl (47). Kinetic parameters were determined by fitting a 1:1 binding model with globally fit parameters for each collected data set

using Biacore T200 Evaluation software (Version 3.2, GE). Owing to the large difference in dissociation rates between the two ligands, only the first 10 s of the dissociation curves were considered for S1-RBD data sets. Quality of fit was determined by agreement between measured and calculated Rmax and chi-squared values. Data sets not producing high-quality kinetic fit were excluded from calculation of kinetic parameters.

Immunofluorescence microscopy

Acid-washed glass coverslips were coated with saturating concentrations of protein (500 nM; S1-RBD or FNIII10) for 1 h at 37 °C. FN-null MEFs (2.5×10^3 cells/cm^2) were seeded in AimV/SF media and incubated at 37 °C, 8% CO_2 for 4 h. Cells were then fixed with 2% paraformaldehyde in PBS and processed for immunofluorescence microscopy as described (107). Cells were incubated with primary antibodies or TRITC-phalloidin diluted in PBS containing 0.1% Tween 20, 1% BSA, and 1 mM phenylmethylsulfonyl fluoride for 1 h at room temperature. Bound antibodies were detected with Alexa^{448}-, Alexa^{549}-, or Alexa^{647}-labeled goat anti-rabbit or -mouse secondary antibodies and visualized using a BX60 fluorescence microscope (Olympus) equipped with an epifluorescent lamp (Lumen Dynamics) and an EXi Blue Fluorescence Camera (Q Imaging), acquired with QCapture software.

Immunoblot analysis

FN-null MEFs (3.4×10^4 cells/cm^2) or SAECs (6.7×10^4 cells/cm^2) were seeded on wells precoated with saturating concentrations of S1-RBD (500 nM), FNIII10 (500 nM), or fibronectin (10 μg/ml) and incubated at 37 °C for 1 h (FN-null MEFs) or 4 h (SAECs). Cells were lysed with 40 μl/cm^2 SDS-RIPA buffer (50 mM Tris, 150 mM NaCl, 1 mM EDTA, 1% Triton X-100, 0.1% sodium dodecyl sulfate, 0.5% sodium deoxycholate, pH 7.6) containing 1 mM sodium orthovanadate, 1 mM phenylmethylsulfonyl fluoride, and 1× protease inhibitor cocktail (Sigma S8830). Cell lysates were analyzed by SDS-PAGE and immunoblotting (108). Immunoblots were blocked with either 5% nonfat milk or 3% BSA in Tris-buffered saline containing 0.1% Tween 20 (TBS-T). Membranes were incubated overnight at 4 °C with primary antibodies diluted in TBS-T. Vinculin was used as the protein loading control. Blots were then washed with TBS-T, incubated with horseradish peroxidase–conjugated secondary antibodies, and developed using SuperSignal West Pico Chemiluminescent Substrate (Thermo Scientific). Blots were imaged using a ChemiDoc imaging system (Bio-Rad).

Bead binding assay

Fc-RBD or mouse IgG (667 nM in PBS) was immobilized on Protein G fluorescent particles (5.0–5.9 μm diameter) according to the manufacturer's instructions. Unbound protein G sites were blocked with 3% BSA. Biotin-labeled 20-mer peptides encompassing the RGD region of SARS-CoV-2 or corresponding KGD region of SARS-CoV-1 were immobilized on streptavidin fluorescent particles (5.0–7.9 μm diameter) according to the manufacturer's instructions and blocked with 1% BSA. Ligand-bound beads were washed and resuspended in small airway epithelial media with or without 1 mM $MnCl_2$ immediately prior to use. Glass coverslips were coated with 10 μg/ml laminin, and SAECs were seeded at a density of 5.4×10^4 cells/cm^2. SAECs were allowed to adhere overnight in growth media and washed twice with basal media immediately prior to bead treatment. SAEC monolayers were incubated with 1×10^6 beads/cm^2 beads for 2 h at 4 °C. Assays were performed at 4 °C to minimize nonspecific endocytosis of particles. Unbound beads were removed by gentle washing with basal media, and cells were fixed with 1% paraformaldehyde in PBS. hSAECs monolayers were visualized by low-power phase microscopy. Cell-bound beads were detected by fluorescence microscopy and counted using FIJI software (NIH, cell counter plugin). The extent of bead binding in each condition was quantified as the mean number of fluorescent beads in 3 to 6 independent regions of interest (0.6 mm^2) per well.

Statistical analysis

Data are presented as mean ± standard error unless otherwise stated. Experiments were performed in duplicate or triplicate on a minimum of two independent days. All statistical analyses were performed using GraphPad Prism (version 9). Statistical differences between groups were identified by two-tailed *t* tests or one- and two-way ANOVAs as indicated, using Bonferroni's posttest and a *p*-value threshold < 0.05.

Data availability

All data are contained within the article, with supplementary data available upon request (denise_hocking@urmc.rochester.edu).

Acknowledgments—The authors thank the University of Rochester Structural Biology and Biophysics Facility for the use of the Biacore T200 System and Dr Jermaine L. Jenkins for technical assistance. This research was supported by National Institutes of Health grant R01 AG058746 and by a University Research Award from the University of Rochester. The content is solely the responsibility of the authors and does not necessarily represent the official views of the National Institutes of Health.

Author contributions—E. G. N. and D. C. H. conceptualization; E. G. N. and D. C. H. data curation; E. G. N. and X. S. P. formal analysis; E. G. N., X. S. P., and D. C. H. investigation; E. G. N. writing - original draft; E. G. N. and D. C. H. writing - review and editing; D. C. H. supervision; D. C. H. funding acquisition; D. C. H. methodology; D. C. H. project administration.

Conflict of interest—The authors declare that they have no conflicts of interest with the contents of this article.

Abbreviations—The abbreviations used are: ACE2, angiotensin-converting enzyme 2; CoV, coronavirus; ECM, extracellular matrix; FAK, focal adhesion kinase; FN-null MEF, fibronectin-null mouse embryonic fibroblast; GST, glutathione S-transferase; RBD, receptor-binding domain; RGD, Arg-Gly-Asp; SAEC, small airway

epithelial cell; SARS, severe acute respiratory syndrome; SPR, surface plasmon resonance.

References

1. Hu, B., Guo, H., Zhou, P., and Shi, Z.-L. (2021) Characteristics of SARS-CoV-2 and COVID-19. *Nat. Rev. Microbiol.* **19**, 141–154
2. Yin, Y., and Wunderink, R. G. (2018) MERS, SARS and other coronaviruses as causes of pneumonia. *Respirology* **23**, 130–137
3. Yuki, K., Fujiogi, M., and Koutsogiannaki, S. (2020) COVID-19 pathophysiology: a review. *Clin. Immunol.* **215**, 108427
4. Bennett, T. D., Moffitt, R. A., Hajagos, J. G., Amor, B., Anand, A., Bissell, M. M., *et al.* (2021) Clinical characterization and prediciton of clinical severity of SARS-CoV-2 infection among US adults using data from the US National COVID Cohort Collaborative. *JAMA Netw. Open* **4**, e2116901
5. Huang, C., Wang, Y., Li, X., Ren, L., Zhao, J., Hu, Y., *et al.* (2020) Clinical features of patients infected with 2019 noval coronavirus in Wuhan, China. *Lancet* **395**, P497–P506
6. Zaim, S., Chong, J. H., Sankaranarayanan, V., and Harky, A. (2020) COVID-10 and multiorgan response. *Curr. Probl. Cardiol.* **45**, 100618
7. Pei, G., Zhang, Z., Peng, J., Liu, L., Zhang, C., Yu, C., *et al.* (2020) Renal involvement and early prognosis in patients with COVID-19 pneumonia. *J. Am. Soc. Nephrol.* **31**, 1157–1165
8. Li, Y., and Xiao, S.-Y. (2020) Hepatic involvement in COVID-19 patients: pathology, pathogenesis, and clinical implications. *J. Med. Virol.* **92**, 1491–1494
9. Pan, L., Mu, M., Yang, P., Sun, Y., Wang, R., Yan, J., *et al.* (2020) Clinical characteristics of COVID-19 patients with digestive symptoms in Hubei, China: a descriptive, cross-sectional, multicenter study. *Am. J. Gastroenterol.* **115**, 766–773
10. Datta, S. D., Talwar, A., and Lee, J. T. (2020) A proposed framework and timeline of the spectrum of disease due to SARS-CoV-2 infection: illness beyond acute infection and public health implications. *JAMA* **324**, 2251–2252
11. Groff, D., Sun, A., Ssentongo, A. E., Ba, D. M., Parsons, N., Poudel, G. R., *et al.* (2021) Short-term and long-term rates of postacute sequelae of SARS-CoV-2 infection: a systematic review. *JAMA Netw. Open* **4**, e2128568
12. Osuchowski, M. F., Wingkler, M. S., Skirecki, T., Cajander, S., Shankar-Hari, M., Lachmann, G., *et al.* (2021) The COVID-19 puzzle: deciphering pathophysiology and phenotypes of a new disease entity. *Lancet Respir. Med.* **9**, 622–642
13. Humphrey, J. D., Dufresne, E. R., and Schwartz, M. A. (2014) Mechanotransduction and extracellular matrix homeostasis. *Nat. Rev. Mol. Cell. Biol.* **15**, 802–812
14. Sakai, T., Larsen, M., and Yamada, K. M. (2003) Fibronectin requirement in branching morphogenesis. *Nature* **423**, 876–881
15. Wheatley, E. M., McKeown-Longo, P. J., Vincent, P. A., and Saba, T. M. (1993) Incorporation of fibronectin into matrix decreases TNF-induced increase in endothelial monolayer permeability. *Am. J. Physiol. Lung Cell. Mol. Physiol.* **265**, L148–L157
16. Curtis, T. M., McKeown-Longo, P. J., Vincent, P. A., Homan, S. M., Wheatley, E. M., and Saba, T. M. (1995) Fibronectin attenuates increased endothelial monolayer permeability after RGD peptide, anti-α5β1, or TNF-α exposure. *Am. J. Physiol.* **269**, L248–L260
17. Hocking, D. C., Titus, P. A., Sumagin, R., and Sarelius, I. H. (2008) Extracellular matrix fibronectin mechanically couples skeletal muscle contraction with local vasodilation. *Circ. Res.* **102**, 372–379
18. Sarelius, I. H., Titus, P. A., Maimon, N., Okech, W., Wilke-Mounts, S. J., Brennan, J. R., *et al.* (2016) Extracellular matrix fibronectin intitates endothelium-dependent arteriolar dilation via the heparin-binding matricryptic RWRPK sequence of the first type III repeat of fibrillar fibronectin. *J. Physiol.* **594**, 687–697
19. Sawicka, K. M., Seeliger, M., Musaev, T., Macri, L. K., and Clark, R. A. F. (2015) Fibronectin interaction and enhancement of growth factors: importance for wound healing. *Adv. Wound Care* **4**, 469–478
20. Vaca, D. J., Thibau, A., Schütz, M., Kraiczy, P., Happonen, L., Malmström, J., *et al.* (2020) Interaction with the host: the role of fibronectin and extracellular matrix proteins in the adhesion of gram-negative bacteria. *Med. Microbiol. Immunol.* **209**, 277–299
21. Mészáros, B., Sámano-Sánchez, H., Alvarado-Valverde, J., Čalyševa, J., Martínez-Pérez, E., Alves, R., *et al.* (2021) Short linear motif candidates in the cell entry system used by SARS-CoV-2 and their potential therapeutic implications. *Sci. Signal.* **14**, eabd0334
22. Ruoslahti, E., and Pierschbacher, M. D. (1987) New perspectives in cell adhesion: RGD and integrins. *Science* **238**, 491–497
23. Pierschbacher, M. D., and Ruoslahti, E. (1984) Cell attachement activity of fibronectin can be duplicated by small synthetic fragments of the molecule. *Nature* **309**, 30–33
24. Larsson, C. (2006) Protein kinase C and the regulation of the actin cytoskeleton. *Cell. Signal.* **18**, 276–284
25. Saoncella, S., Echtermeyer, F., Denhez, F., Nowlen, J. K., Mosher, D. F., Robinson, S. D., *et al.* (1999) Syndecan-4 signals cooperatively with integrins in a Rho-dependent manner in the assembly of focal adhesions and actin stress fibers. *Proc. Natl. Acad. Sci. U. S. A.* **96**, 2805–2810
26. Longley, R. L., Woods, A., Fleetwood, A., Cowling, G. J., Gallagher, J. T., and Couchman, J. R. (1999) Control of morphology, cytoskeleton and migration by syndecan-4. *J. Cell Sci.* **112**, 3421–3431
27. Singh, P., Carraher, C., and Schwarzbauer, J. E. (2010) Assembly of fibronectin extracellular matrix. *Annu. Rev. Cell. Dev. Biol.* **26**, 397–419
28. Citalán-Madrid, A. F., Vargas-Robles, H., García-Ponce, A., Shibayama, M., Betanzos, A., Nava, P., *et al.* (2017) Cortactin deficiency causes increased RhoA/ROCK1-dependent actomyosin contractility, intestinal epithelial barrier dysfunction, and disproportionately severe DSS-induced colitis. *Mucosal Immunol.* **10**, 1237–1247
29. Walls, A. C., Park, Y.-J., Tortorici, M. A., Wall, A., McGuire, A. T., and Veesler, D. (2020) Structure, function, and antigenicity of the SARS-CoV-2 spike glycoprotein. *Cell* **181**, 281–292
30. Lamers, M., Beumer, J., van der Vaart, J., Knoops, K., Pushchhof, J., Breugem, T. I., *et al.* (2020) SARS-CoV-2 productively infects human gut enterocytes. *Science* **369**, 50–54
31. Hoffmann, M., Kleine-Weber, H., Schroeder, S., Kruger, N., Herrler, T., Erichsen, S., *et al.* (2020) SARS-CoV-2 cell entry depends on ACE2 and TMPRSS2 and is blocked by a clinically proven protease inhibitor. *Cell* **181**, 271–280.e8
32. Lan, J., Ge, J., Yu, J., Shan, S., Zhou, H., Fan, S., *et al.* (2020) Structure of the SARS-CoV-2 spike receptor-binding domain bound to the ACE2 receptor. *Nature* **581**, 215–220
33. Zech, F., Schniertshauer, D., Jung, C., Herrmann, A., Cordsmeier, A., Xie, Q., *et al.* (2021) Spike residue 403 affects binding of coronavirus spikes to human ACE2. *Nat. Commun.* **12**, 6855
34. Beddingfield, B. J., Iwanaga, N., Chapagain, P. P., Zheng, W., Roy, C. J., Hu, T. Y., *et al.* (2021) The integrin binding peptide ATN-161, as a novel therapy for SARS-CoV-2 infection. *JACC Basic Transl. Sci.* **6**, 1–8
35. Robles, J. P., Zamora, M., Adan-Castro, E., Siqueiros-Marquez, L., de la Escalera, G. M., and Clapp, C. (2022) The spike protein of SARS-CoV-2 induces endothelial inflammation through integrin a5B1 and NF-kB signaling. *J. Biol. Chem.* **298**, 101695
36. Nader, D., Fletcher, N., Curley, G. F., and Kerrigan, S. W. (2021) SARS-CoV-2 uses major endothelial integrin aVB3 to cause vascular dysregulation *in vitro* during COVID-19. *PLoS One* **16**, e0253347
37. Amruta, N., Engler-Chiurazzi, E. B., Murray-Brown, E. C., Gressett, T. E., Biose, I. J., Chastain, W. H., *et al.* (2021) *In vivo* protection from SARS-CoV-2 infection by ATN-161 in k18-hACE2 transgenic mice. *Life Sci.* **284**, 119881
38. Simons, P., Rinaldi, D. A., Bondu, V., Kell, A., Bradfute, S., Lidke, D. S., *et al.* (2021) Integrin activation is an essential component of SARS-CoV-2 infection. *Sci. Rep.* **11**, 20398
39. Wojciechowski, K., Chang, C. H., and Hocking, D. C. (2004) Expression, production, and characterization of full-length vitronectin in Escherichia coli. *Protein Expr. Purif.* **36**, 131–138
40. Sottile, J., Hocking, D. C., and Swiatek, P. J. (1998) Fibronectin matrix assembly enhances adhesion-dependent cell growth. *J. Cell Sci.* **111**, 2933–2943

41. Roy, D. C., and Hocking, D. C. (2013) Recombinant fibronectin matrix mimetics specify integrin adhesion and extracellular matrix assembly. *Tissue Eng. Part A* **19**, 558–570
42. Sottile, J., and Hocking, D. C. (2002) Fibronectin polymerization regulates the composition and stability of extracellular matrix fibrils and cell-matrix adhesions. *Mol. Biol. Cell* **13**, 3546–3559
43. Humphries, J. D., Byron, A., and Humphries, M. J. (2006) Integrin ligands at a glance. *J. Cell Sci.* **119**, 3901–3903
44. Murphy, K. N., and Brinkworth, A. J. (2021) Manipulation of focal adhesion signaling by pathogenic microbes. *Int. J. Mol. Sci.* **22**, 1358
45. Burridge, K., and Chrzanowska-Wodnicka, M. (1996) Focal adhesions, contractility, and signaling. *Annu. Rev. Cell. Dev. Biol.* **12**, 463–519
46. Farrar, C. S., Rouin, G. T., Miller, B. L., Raeman, C. H., Mooney, N. A., and Hocking, D. C. (2019) A matricryptic conformation of the integrin-binding domain of fibronectin regulates platelet-derived growth factor-induced intracellular calcium release. *Cells* **8**, 1351
47. Brown, A. C., Dysart, M. M., Clarke, K. C., Stabenfeldt, S. E., and Barker, T. H. (2015) Integrin α3β1 binding to fibronectin Is dependent on the ninth type III repeat. *J. Biol. Chem.* **290**, 25534–25547
48. Harburger, D. S., and Calderwood, D. A. (2009) Integrin signaling at a glance. *J. Cell Sci.* **122**, 159–163
49. Burridge, K. (2017) Focal adhesions: a personal perspective on a half century of progress. *FEBS J.* **284**, 3355–3361
50. Geiger, B., Bershadsky, A., Pankov, R., and Yamada, K. M. (2001) Transmembrane extracellular matrix-cytoskeleton crosstalk. *Nat. Rev. Mol. Cell. Biol.* **2**, 793–805
51. Schaller, M. D., Hildebrand, J. D., Shannon, J. D., Fox, J. W., Vines, R. R., and Parsons, J. T. (1994) Autophosphorylation of the focal adhesion kinase, pp125FAK, directs SH2-dependent binding of pp60Src. *Mol. Cell. Biol.* **14**, 1680–1688
52. Cobb, B. S., Schaller, M. D., Leu, T.-H., and Parsons, J. T. (1994) Stable association of pp60src and pp59fyn with the focal adhesion-associated protein tyrosine kinase, pp125FAK. *Mol. Cell. Biol.* **14**, 147–155
53. Calalb, M. B., Polte, T. R., and Hanks, S. K. (1995) Tyrosine phosphorylation of focal adhesion kinase at sites in the catalytic domain regulates kinase activity: a role for src family kinases. *Mol. Cell. Biol.* **15**, 954–963
54. Schaller, M. D., and Parsons, J. T. (1995) pp125FAK-dependent tyrosine phosphorylation of paxillin creates a high-affinity binding site for Crk. *Mol. Cell. Biol.* **15**, 2635–2645
55. Turner, C. E. (2000) Paxillin and focal adhesion signaling. *Nat. Cell Biol.* **2**, E231–E236
56. Troussard, A. A., Mawji, N. M., Ong, C., Mui, A., St.-Arnaud, R., and Dedhar, S. (2003) Conditional knock-out of integrin-linked kinase demonstrates an essential role in protein kinase B/Akt activation. *J. Biol. Chem.* **278**, 22374–22378
57. Khwaja, A., Rodriguez-Viciana, P., Wennström, S., Warne, P. H., and Downward, J. (1997) Matrix adhesion and Ras transformation both activate a phosphoinositide 3-OH kinase and protein kinase B/Akt cellular survival pathway. *EMBO J.* **16**, 2783–2793
58. Hocking, D. C., Sottile, J., and McKeown-Longo, P. J. (1994) Fibronectin's III-1 module contains a conformation-dependent binding site for the amino-terminal region of fibronectin. *J. Biol. Chem.* **269**, 19183–19191
59. Sun, X., Skorstengaard, K., and Mosher, D. F. (1992) Disulfides modulate RGD-inhibitable cell adhesive activity of thrombospondin. *J. Cell Biol.* **118**, 693–701
60. Cluzel, C., Saltel, F., Lussi, J., Paulhe, F., Imhof, B. A., and Wehrle-Haller, B. (2005) The mechanisms and dynamics of αvβ3 integrin clustering in living cells. *J. Cell Biol.* **171**, 383–392
61. Posch, W., Vosper, J., Noureen, A., Zaderer, V., Witting, C., Bertacchi, G., *et al.* (2021) C5aR inhibition of nonimmune cells suppresses inflammation and maintains epithelial integrity in SARS-CoV-2-infected primary human airway epithelia. *J. Allergy Clin. Immunol.* **147**, 2083–2097
62. Wettstein, L., Weil, T., Conzelmann, C., Müller, J. A., Groß, R., Hirschenberger, M., *et al.* (2021) Alpha-1 antitrypsin inhibits TMPRSS2 protease activity and SARS-CoV-2 infection. *Nat. Commun.* **12**, 1726
63. Scarborough, R. M., Rose, J. W., Hsu, M. A., Phillips, D. R., Fried, V. A., Campbell, A. M., *et al.* (1991) Barbourin. A GPIIb-IIIa-specific integrin antagonist from the venom of Sistrurus m. barbouri. *J. Biol. Chem.* **266**, 9359–9362
64. Huang, J., Li, X., Shi, X., Zhu, M., Wang, J., Huang, S., *et al.* (2019) Platelet integrin alphaIIbbeta3: signal transduction, regulation, and its therapeutic targeting. *J. Hematol. Oncol.* **12**, 26
65. Park, E. J., Myint, P. K., Gyasi, A. M., Darkway, S., Caidengbate, S., Ito, A., *et al.* (2021) The spike glycoprotein of SARS-CoV-2 binds to β1 integrins expressed on the surface of lung epithelial cells. *Viruses* **13**, 645
66. Clarke, N. E., Fisher, M. J., Porter, K. E., Lambert, D. W., and Turner, A. J. (2012) Angiotensin converting enzyme (ACE) and ACE2 bind integrins and ACE2 regulates integrin signaling. *PLoS One* **7**, e34747
67. Lin, Q., Keller, R. S., Weaver, B., and Zisman, L. S. (2004) Interaction of ACE2 and integrin β1 in failing human heart. *Biochim. Biophys. Acta* **1689**, 175–178
68. Liu, J., Lu, F., Chen, Y., Plow, E., and Qin, J. (2022) Integrin mediates cell entry of the SARS-CoV-2 virus independent of cellular receptor ACE2. *J. Biol. Chem.* **298**, 101710
69. Bugatti, A., Filippini, F., Bardelli, M., Zani, A., Chiodelli, P., Messali, S., *et al.* (2022) SARS-CoV-2 infects human ACE2-negative endothelial cells through an αvβ3 integrin-mediated endocytosis even in the presence of vaccine-elicited neutralizing antibodies. *Viruses* **14**, 705
70. Pytela, R., Pierschbacher, M. D., Argraves, S., Suzuki, S., and Ruoslahti, E. (1987) Arginine-glycine-aspartic acid adhesion receptors. *Methods Enzymol.* **144**, 475–489
71. Mould, A. P., Askari, J. A., Barton, S., Kline, A. D., McEwan, P. A., Craig, S. E., *et al.* (2002) Integrin activation involves a conformational change in the α1 helix of the β subunit A-domain. *J. Biol. Chem.* **277**, 19800–19805
72. Woods, A. (2001) Syndecans: transmembrane modulators of adhesion and matrix assembly. *J. Clin. Invest.* **107**, 935–941
73. van Hinsbergh, V. W. M., Engelse, M., and Quax, P. H. A. (2006) Pericellular proteases in angiogenesis and vasculogenesis. *Arterioscler. Thromb. Vasc. Biol.* **26**, 716–728
74. Clausen, T. M., Sandoval, D. R., Spliid, C. B., Pihl, J., Perrett, H. R., Painter, C. D., *et al.* (2020) SARS-CoV-2 infection depends on cellular heparan sulfate and ACE2. *Cell* **183**, 1043–1057
75. Zhao, M.-M., Yang, W.-L., Yang, F.-Y., Zhang, L., Huang, W.-J., Hou, W., *et al.* (2021) Cathepsin L plays a key role in SARS-CoV-2 infection in humans and humanized mice and is a promising target for new drug development. *Signal. Transduct. Target. Ther.* **6**, 134
76. Othman, H., Messaoud, H. B., Khamessi, O., Ben-Mabrouk, H., Ghedira, K., Bharuthram, A., *et al.* (2022) SARS-CoV-2 spike protein unlikely to bind to integrins via the Arg-Gly-Asp (RGD) motif of the receptor binding domain: evidence from structural analysis and microscale accelerated molecular dynamics. *Front. Mol. Biosci.* **9**, 834857
77. Hotchkiss, K. A., Matthias, L. J., and Hogg, P. J. (1998) Exposure of the cryptic Arg-Gly-Asp sequence in thrombospondin-1 by protein disulfide isomerase. *Biochim. Biophys. Acta* **1388**, 478–488
78. Zhong, C., Chrzanowska-Wodnicka, M., Brown, J., Shaub, A., Belkin, A., and Burridge, K. (1998) Rho-mediated contractility exposes a cryptic site in fibronectin and induces fibronectin matrix assembly. *J. Cell Biol.* **141**, 539–551
79. Wrapp, D., Wang, N., Corbett, K. S., Goldsmith, J. A., Hsieh, C.-L., Abiona, O., *et al.* (2020) Cryo-EM structure of the 2019-nCoV spike in the prefusion conformation. *Science* **367**, 1260–1263
80. Turoňová, B., Sikora, M., Schürmann, C., Hagen, W. J., Welsch, S., Blanc, F. E., *et al.* (2020) *In situ* structural analysis of SARS-CoV-2 spike reveals flexibility mediated by three hinges. *Science* **379**, 203–208
81. Ray, D., Le, L., and Andricioaei, I. (2021) Distant residues modulate conformational opening in SARS-CoV-2 spike protein. *Proc. Natl. Acad. Sci. U. S. A.* **118**, e21009
82. Liu, L., Chopra, P., Li, X., Bouwman, K. M., Tompkins, S. M., Wolfert, M. A., *et al.* (2021) Heparin sulfate proteoglycans as attachment factor for SARS-CoV-2. *ACS Cent. Sci.* **7**, 1009–1018

83. Couchman, J. R., and Woods, A. (1999) Syndecan-4 and integrins: combinatorial signaling in cell adhesion. *J. Cell Sci.* **112**, 3415–3420
84. Woods, A., and Couchman, J. R. (1994) Syndecan 4 heparan sulfate proteoglycan is a selectively enriched and widewpread focal adhesion component. *Mol. Biol. Cell* **5**, 183–192
85. Carvacho, I., and Piesche, M. (2021) RGD-binding integrins and TGF-β in SARS-CoV-2 infections - novel targets to treat COVID-19 patients? *Clin. Transl. Immunol.* **10**, e1240
86. Feire, A. L., Koss, H., and Compton, T. (2004) Cellular integrins function as entry receptors for human cytomegalovirus via a highly conserved disintegrin-like domain. *Proc. Natl. Acad. Sci. U. S. A.* **101**, 15470–15475
87. Gavrilovskaya, I. N., Brown, E. J., Ginsberg, M. H., and Mackow, E. R. (1999) Cellular entry of hantaviruses which cause hemorrhagic fever with renal syndrome is mediated by β3 integrins. *J. Virol.* **73**, 3951–3959
88. Meliopoulos, V. A., Van de Velde, L.-A., Van de Velde, N. C., Karlsson, E. A., Neale, G., Vogel, P., *et al.* (2016) An epithelial integrin regulates the amplitude of protective lung interferon responses against multiple respiratory pathogens. *PLoS Pathog.* **12**, e1005804
89. Yan, S., Sun, H., Bu, X., and Wan, G. (2020) New strategy for COVID-10. An evolutionary role for RGD motif in SARS-CoV-2 and potential inhibitors for virus infection. *Front. Pharmacol.* **11**, 912
90. Harvey, W. T., Carabelli, A. M., Jackson, B., Gupta, R. K., Thomson, E. C., Harrison, E. M., *et al.* (2021) SARS-CoV-2 variants, spike mutations and immune escape. *Nat. Rev. Microbiol.* **19**, 409–424
91. Beyerstedt, S., Casaro, E. B., and Rangel, É. B. (2021) COVID-19: angiotensin-converting enzyme 2 (ACE2) expression and tissue susceptibility to SARS-CoV-2 infection. *Eur. J. Clin. Microbiol. Infect. Dis.* **40**, 905–919
92. Cohler, L. F., Saba, T. M., Lewis, E., Vincent, P. A., and Charash, W. E. (1987) Plasma fibronectin therapy and lung protein clearance with bacteremia after surgery. *J. Appl. Physiol.* **63**, 623–633
93. Curtis, T. M., Rotundo, R. F., Vincent, P. A., McKeown-Longo, P. J., and Saba, T. M. (1998) TNF-α-induced matrix Fn disruption and decreased endothelial integrity are independent of Fn proteolysis. *Am. J. Physiol. Lung Cell. Mol. Physiol.* **275**, L126–L138
94. Rotundo, R. F., Curtis, T. M., Shah, M. D., Gao, B., Mastrangelo, A., LaFlamme, S. E., *et al.* (2002) TNF-α disruption of lung endothelial integrity: reduced integrin mediated adhesion to fibronectin. *Am. J. Physiol. Lung Cell. Mol. Physiol.* **282**, L316–L329
95. Resnikoff, M., Brien, T., Vincent, P. A., Rotundo, R. F., Lewis, E., McKeown-Longo, P. J., *et al.* (1999) Lung matrix incorporation of plasma fibronectin reduces vascular permeability in postsurgical bacteremia. *Am. J. Physiol. Lung Cell. Mol. Physiol.* **277**, L749–L759
96. Roth, T., Podestá, F., Stepp, M. A., Boeri, D., and Lorenzi, M. (1993) Integrin overexpression induced by high glucose and by human diabetes: potential pathyway to cell dysfunction in diabetic microangiopathy. *Proc. Natl. Acad. Sci. U. S. A.* **90**, 9640–9644
97. Kitsiou, P. V., Tzinia, A. K., Stetler-Stevenson, W. G., Michael, A. F., Fan, W.-W., Zhou, B., *et al.* (2003) Glucose-induced changes in integrin and matrix related functions in cultured human glomerular epithelial cells. *Am. J. Physiol. Ren. Physiol.* **284**, F671–F679
98. Kim, C. H., and Vaziri, N. D. (2005) Hypertension promotes integrin expression and reactive oxygen species generation by circulating leukocytes. *Kidney Int.* **67**, 1462–1470
99. Burgess, M. L., Terracio, L., Hirozane, T., and Borg, T. K. (2002) Differential integrin expression by cardiac fibroblast from hypertensive and exercise-trained rat hearts. *Cardiovasc. Pathol.* **11**, 78–87
100. Umesh, A., Paudel, O., Cao, Y.-N., Myers, A. C., and Sham, J. S. (2011) Alteration of pulmonary artery integrin levels in chronic hypoxia and monocrolatine-induced pulmonary hypertension. *J. Vasc. Res.* **48**, 525–537
101. Mezu-Ndubuisi, O. J., and Maheshwari, A. (2020) The role of integrins in inflammation and angiogeneisis. *Pediatr. Res.* **89**, 1619–1626
102. Akiyama, S. K. (2013) Purification of fibronectin. *Curr. Protoc. Cell Biol.* **60**, 10.15.11-10.15.13
103. Hocking, D. C., Smith, R. K., and McKeown-Longo, P. J. (1996) A novel role for the integrin-binding III10 module in fibronectin matrix assembly. *J. Cell Biol.* **133**, 431–444
104. Sottile, J., Shi, F., Rublyevska, I., Chiang, H.-Y., Lust, J., and Chandler, J. (2007) Fibronectin-dependent collagen I deposition modulates the cell response to fibronectin. *Am. J. Physiol. Cell Physiol.* **293**, C1934–C1946
105. Pereira, M., Rybarczyk, B. J., Odrljin, T. M., Hocking, D. C., Sottile, J., and Simpson-Haidaris, P. J. (2002) The incorporation of fibrinogen into extracellular matrix is dependent on active assembly of a fibronectin matrix. *J. Cell Sci.* **115**, 609–617
106. Roy, D. C., Wilke-Mounts, S., and Hocking, D. C. (2011) Chimeric fibronectin matrix mimetic as a functional growth- and migration-promoting adhesive substrate. *Biomaterials* **32**, 2077–2087
107. Hocking, D. C., and Kowalski, K. (2002) A cryptic fragment from fibronectin's III1 module localizes to lipid rafts and stimulates cell growth and contractility. *J. Cell Biol.* **158**, 175–184
108. Gildner, C. D., Roy, D. C., Farrar, C. S., and Hocking, D. C. (2014) Opposing effects of collagen I and vitronectin on fibronectin fibril structure and function. *Matrix Biol.* **34**, 33–45